Supporting Information

Optical Actuation of Nanoparticle-Loaded Liquid-Liquid Interfaces for Active Photonics

Youngsun Kim[1], Kan Yao[1,2], Carolina Ponce[2], Yuebing Zheng[1,2]*

[1]Materials Science and Engineering Program, Texas Materials Institute, The University of Texas at Austin, Austin, Texas 78712, USA

[2]Walker Department of Mechanical Engineering, The University of Texas at Austin, Austin, Texas 78712, USA

*Corresponding author. Email: zheng@austin.utexas.edu

Contents

Figures S1-19

Notes S1-6

Captions for Movies S1-7

References

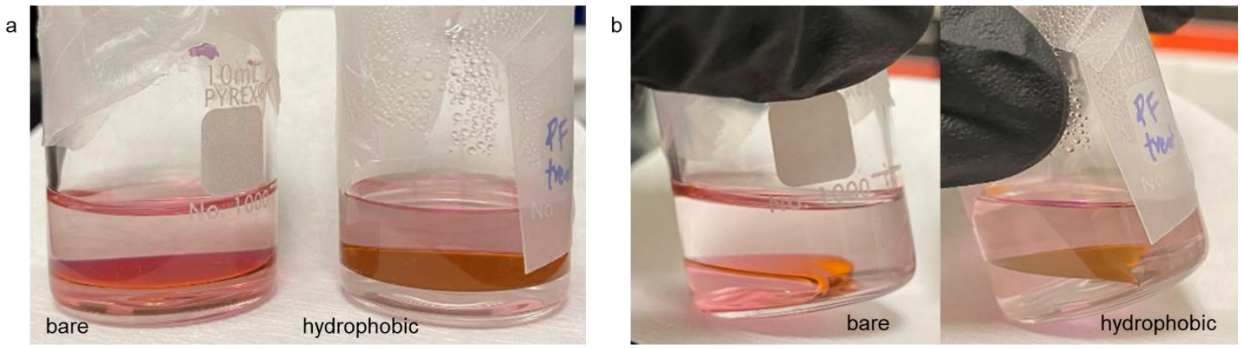

Figure S1. (a) Biphasic liquid systems prepared in bare and hydrophobically modified glass beakers. The hydrophobically treated beaker displays a nearly flat interface near the glass surfaces, which is more evident when the beaker is tilted (b).

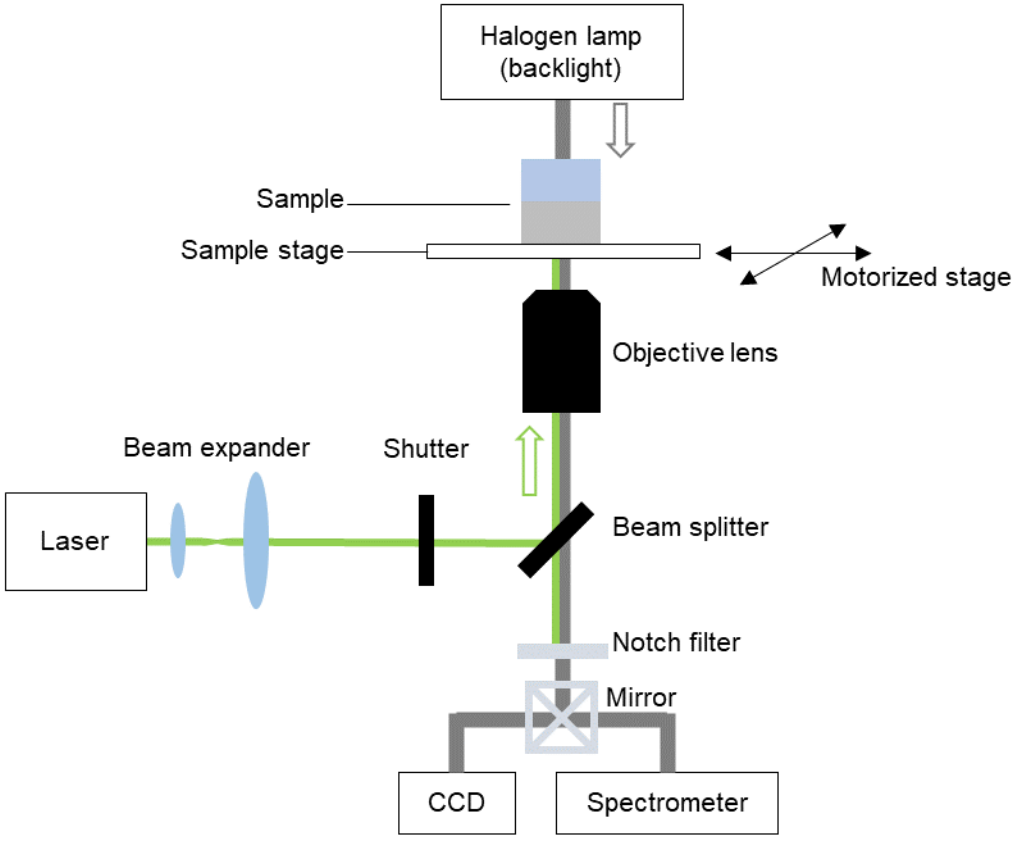

Figure S2. Optical setup for optical microscopy and *in situ* spectroscopy.

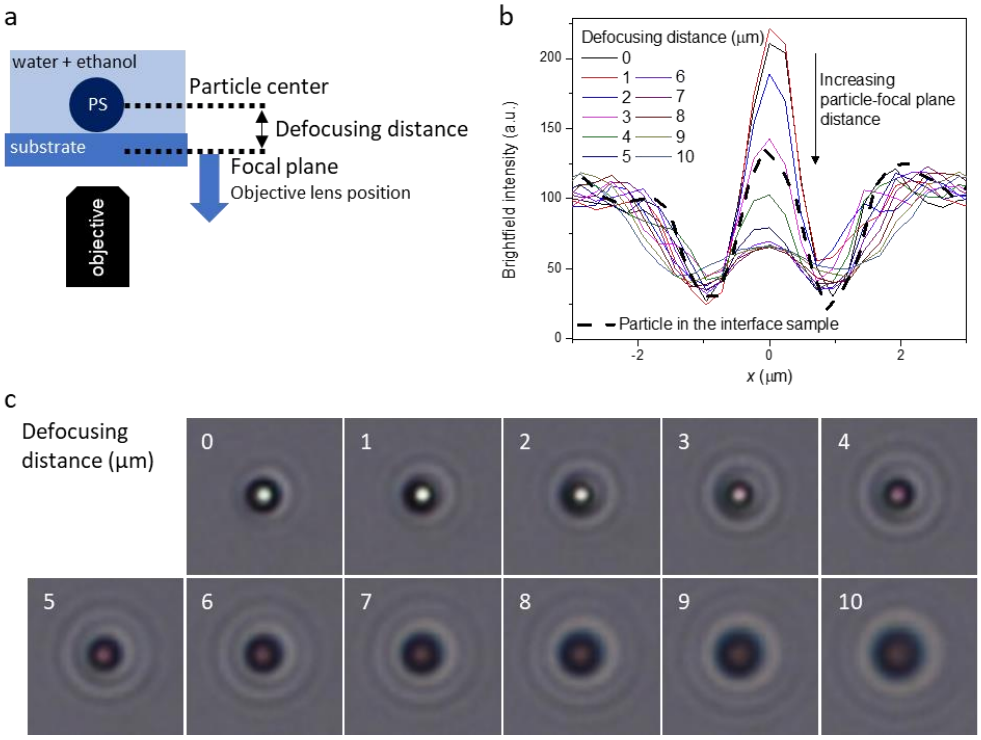

Figure S3. (a) Schematic illustration validating the vertical position of a PS microparticle. (b) Brightfield image intensity profile along the *x*-axis. (c) Corresponding microscopic images of a PS particle at varying defocusing distances.

Note S1. Approximation of the incident angle factor in Eq. 2 and full equation of the radiation pressure

As the radiation pressure, Π_{rad} is defined as the intensity of radiation force normal to the interface, $\Pi_{rad}(r)$ along the curved interface depends on the local incident angle (α_i) of the beam. This angle-dependent term $f(\alpha_i)$ is written as[1,2]

$$f(\alpha_i) = \frac{\cos^2(\alpha_i)}{\delta}\left(1 + R - \frac{\tan\alpha_i}{\tan\left(\arcsin\left(n_1 \sin\alpha_i / n_2\right)\right)}T\right), \qquad \text{(Eq. S1)}$$

where R and T are the reflectance and transmittance, respectively ($R + T = 1$), and δ is the relative difference of refractive indices, $2(n_2 - n_1)/(n_1 + n_2)$. In the case of relatively small δ (< 0.1), $f(\alpha_i)$ can be approximated as[1]

$$f(\alpha_i) \approx \begin{cases} 2\left(\theta_i/\sqrt{\delta}\right)^2 & \left(\theta_i < \sqrt{2\delta}\right) \\ \dfrac{4\left(\theta_i/\sqrt{\delta}\right)^2}{\left(\theta_i/\sqrt{\delta} + \sqrt{-2 + \left(\theta_i/\sqrt{\delta}\right)^2}\right)^2} & \left(\theta_i > \sqrt{2\delta}\right) \end{cases} \qquad \text{(Eq. S2)}$$

where θ_i is the complementary angle ($\pi/2 - \alpha_i$) that can be described by the first derivative of interface profile $h(r)$ as $\arctan(1/h'(r))$. Total reflection occurs when $\theta_i = \sqrt{2\delta}$.

With this approximation, a full equation of the radiation pressure is written as follows (Eq. S3).

$$\Pi_{rad}(r) = \begin{cases} -\dfrac{4n_1 P}{c\pi\omega_0^2\left[1 + \left(h(r)/z_R\right)^2\right]} \exp\left(-\dfrac{2r^2}{\omega_0^2\left[1 + \left(h(r)/z_R\right)^2\right]}\right) \arctan^2\left(1/h'(r)\right) & \left(\arctan\left(1/h'(r)\right) > \sqrt{2\delta}\right) \\ -\dfrac{4n_1 P}{c\pi\omega_0^2\left[1 + \left(h(r)/z_R\right)^2\right]} \exp\left(-\dfrac{2r^2}{\omega_0^2\left[1 + \left(h(r)/z_R\right)^2\right]}\right) \dfrac{2\arctan^2\left(1/h'(r)\right)}{\left[\left(\arctan\left(1/h'(r)\right)/\sqrt{\delta} + \sqrt{-2 + \left(\arctan\left(1/h'(r)\right)/\sqrt{\delta}\right)^2}\right)\right]^2} & \left(\arctan\left(1/h'(r)\right) < \sqrt{2\delta}\right) \end{cases}$$

The numerical solutions of the force balance equation (Eq. 1) with a boundary condition $h'(0) = 0$, are shown in Figure S4 ($\Delta\rho$ = 460 kg m^{-3}, n_1 = 1.29, n_2 = 1.36).

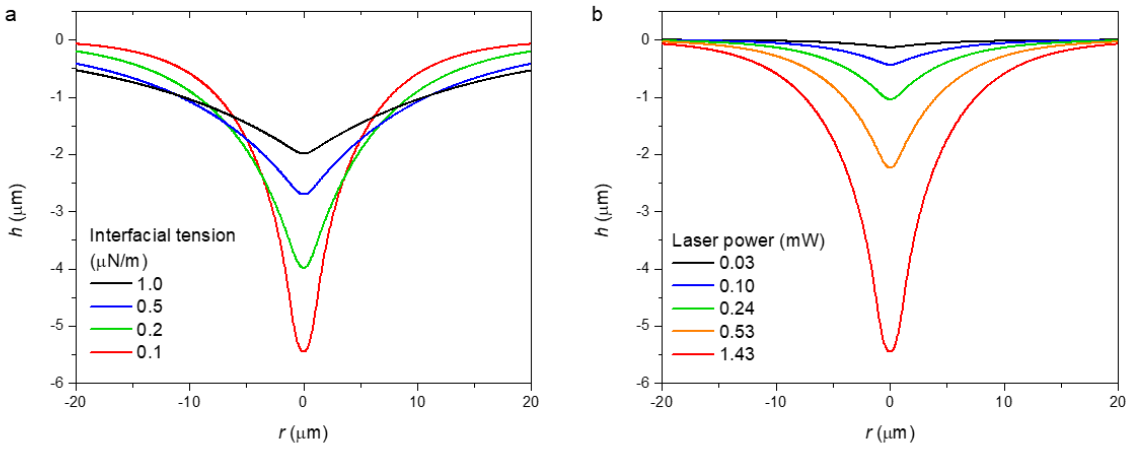

Figure S4. Interface deformation profiles of the bare liquid-liquid system (a) with varying interfacial tensions at a laser power of 1.43 mW and (b) at varying laser powers with an interfacial tension of 0.1 μN/m.

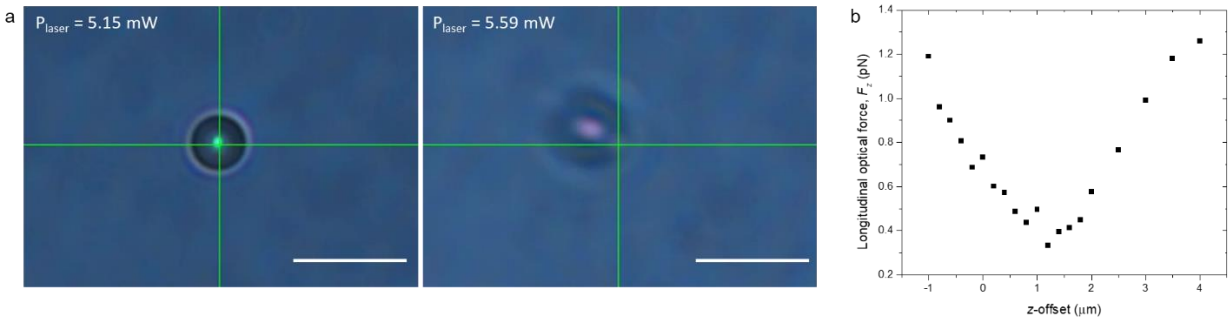

Figure S5. (a) Trapping (left)-to-pushing (right) transition of a PS particle with a tightly focused laser beam (NA 1.3). Scale bars: 5 μm. (b) Simulated optical force for a PS particle at the transition optical power (5.37 mW) by the high-NA laser beam at varying z-offsets from the laser beam.

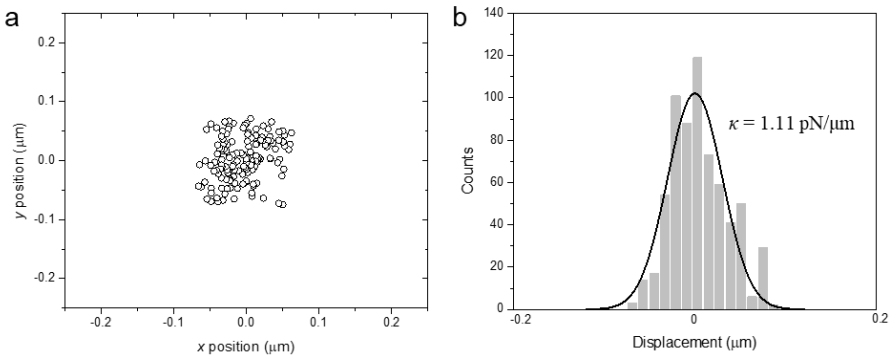

Figure S6. (a) The trajectory of a PS particle trapped at 1.43 mW. (b) Histogram of the measured displacements from the beam center. The trapping stiffness of the particle was calculated as k_BT/σ^2, where k_B is the Boltzmann constant, T is the temperature, and σ is the standard deviation of the Gaussian fit for the histogram.

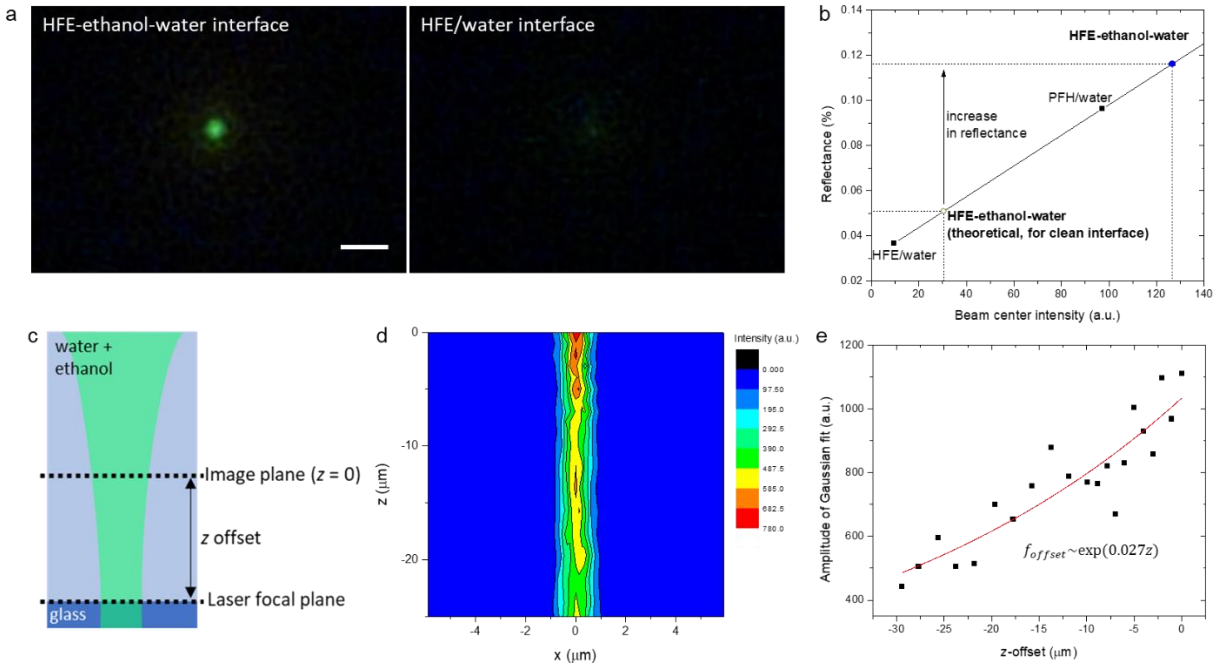

Figure S7. (a) Microscopic images of a laser beam at HFE-ethanol-water and HFE/water interfaces. Scale bars: 5 μm. (b) Scaled reflectance from center beam intensity and theoretical reflectance from $(n_1 - n_2)^2/(n_1 + n_2)^2$. Refractive indices used in the calculation are 1.28 (HFE), 1.25 (PFH) and 1.33 (water) for the binary systems, and 1.36 (top phase) and 1.29 (bottom phase) for the ternary system. The refractive index of the bottom phase in the ternary system was calculated using the Arago−Biot equation[3] with volume fractions of 0.87 and 0.13 for HFE and ethanol, respectively. The volume fractions were obtained from the measured density reduction (1.32 from 1.40 g/mL) and the volume reduction upon mixing of HFE and ethanol was found negligible. Attenuation of the laser beam by the interface deformation was accounted using the Gaussian beam equation and the interface profile of the bare liquid-liquid interface. Additionally, another attenuation factor due to the *z*-offset of the interface from the image plane was incorporated using the measured laser beam profile with respect to the *z*-offset (c-e).

Note S2. Phase behavior of HFE, ethanol and water mixture

The ternary liquid system (HFE, ethanol and water) shows phase behavior different from binary immiscible liquid systems. Upon addition of water to HFE-ethanol mixture, the mixture immediately becomes cloudy due to the formation of emulsions (Figure S8a). The observed volume change indicates that ethanol is extracted to water, forming the top phase of water and ethanol, and leaving the bottom phase of HFE. Over time, the cloudy portion of the two phases move to the interface and eventually both phases turn transparent. In comparison, a binary system of HFE and water shows no cloudy appearance upon mixing (Figure S8b). This phase behavior implies a self-surfactant role of the liquids. HFE has an amphiphilic chemical structure, possessing a perfluorocarbon chain and an ethyl ether group (Figure S8c). As the perfluorocarbon group has limited miscibility with both hydrocarbon and polar liquids, the two contrasting groups in one structure may endow HFE with the amphiphilic property as well as its miscibility with ethanol. Ethanol has miscibility with both HFE and water, and higher affinity to water according to the extraction behavior. Thus, its ethyl group tends to interface with the ethyl ether group of HFE while its hydroxyl group interacts with water. With these considerations, a possible scenario of interfacial arrangement is in order of HFE, ethanol and water. Taken together with the presence of microscale HFE droplets on the interface (Movie S3), the molecular arrangement contributes to the formation of HFE-rich emulsions. We attribute this emulsion phase at the interface to the low interfacial tension. It was noted that the formation of stable emulsion phase is also shown in several binary liquid systems without additional surfactant[4–6].

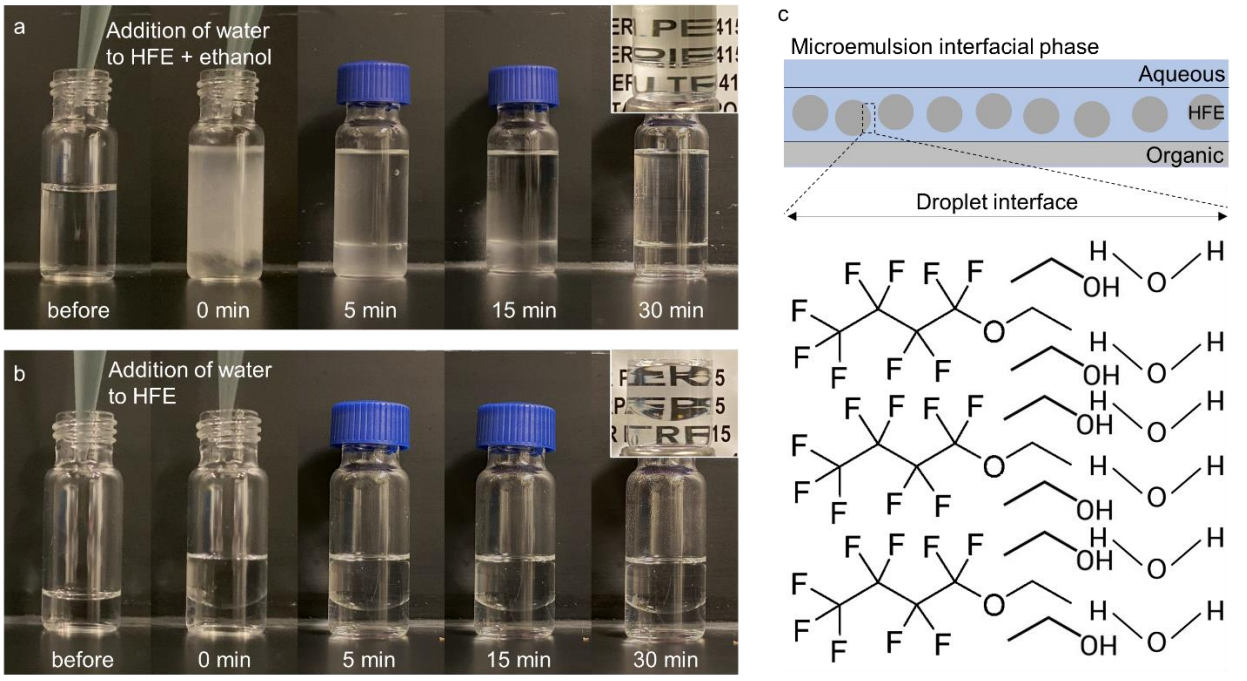

Figure S8. (a,b) Temporal evolution of (a) HFE-ethanol-water ternary liquid system and (b) HFE-water binary liquid system. (c) Chemical structures of HFE, ethanol, and water and the possible scenario of their interfacial arrangement.

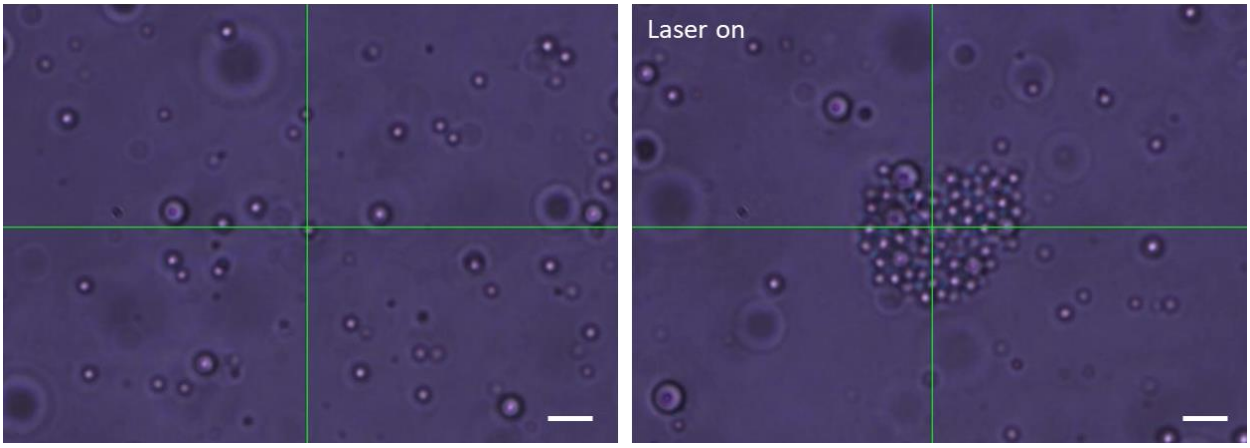

Figure S9. Optothermal accumulation of PFP droplets in a water-ethanol mixture (50 vol%) on a 4.5 nm gold nanoislands substrate (scale bars: 5 µm).

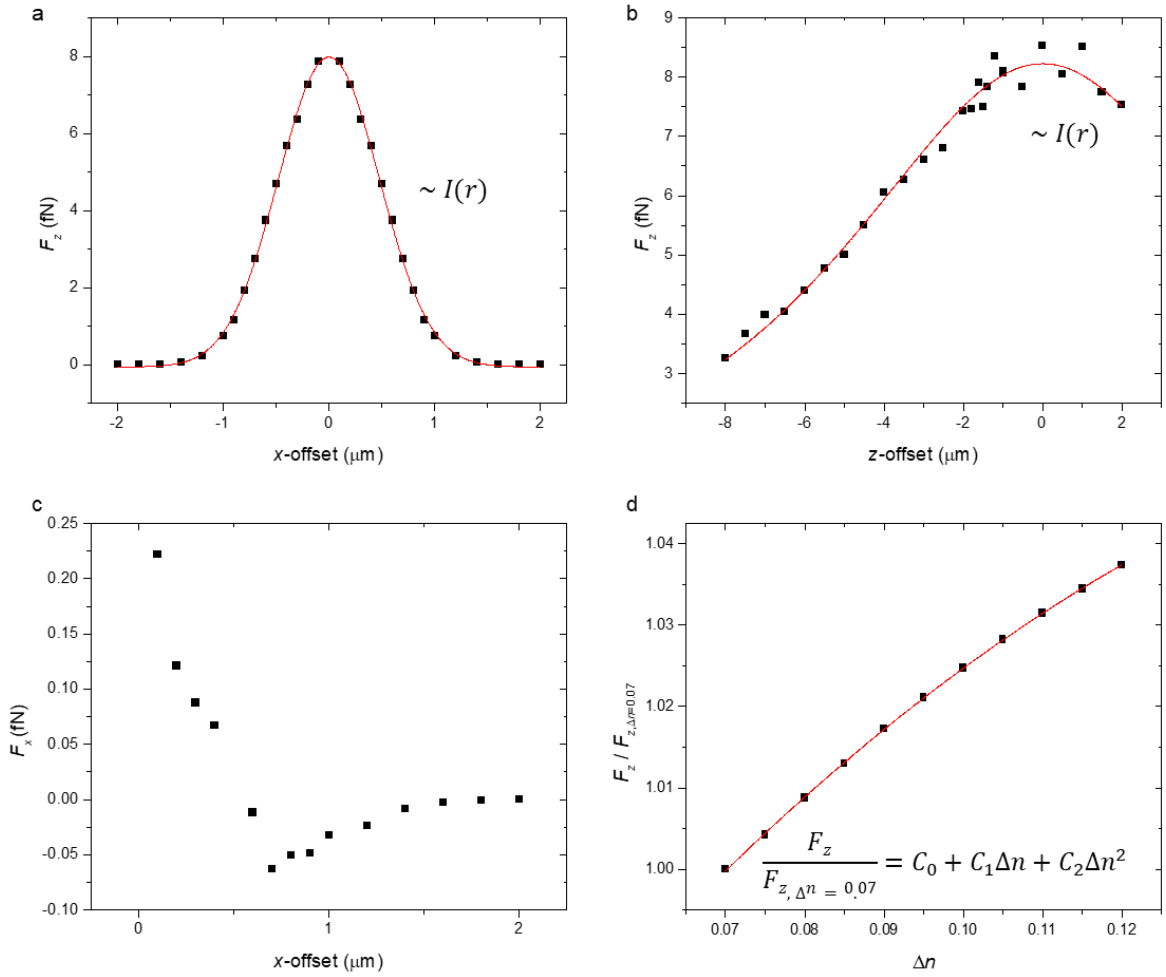

Figure S10. Simulated optical force for an Au NP: longitudinal force F_z with respect to (a) x-offset and (b) z-offset of the particle from the beam center, and (c) transverse force F_x with respect to x-offset. (d) Relative F_z with respect to refractive index contrast. $I(r)$ is the Gaussian beam equation in Eq. 2.

Note S3. Spectral simulation of Au NP hexagonal arrays

Transmittance, reflectance and absorptance spectra of the interfacial gold film with respect to interparticle spacing *s* were simulated using a model of nanoparticle hexagonal array (finite-element solver, COMSOL Multiphysics). A unit cell of hexagonal lattice (Figure S11a) was constructed, and a periodic boundary condition with Floquet periodicity was applied at the side boundaries of the unit cell. A linearly polarized light source was implemented at the top boundary of the unit cell (input port) and the bottom boundary was set as the output port. Both ports were backed by perfectly matched layers (PMLs). To obtain complete spectra, the wavelengths were swept with a step of 10 nm. Please note the possibility of over/underestimation as a perfect array was used without considering defects.

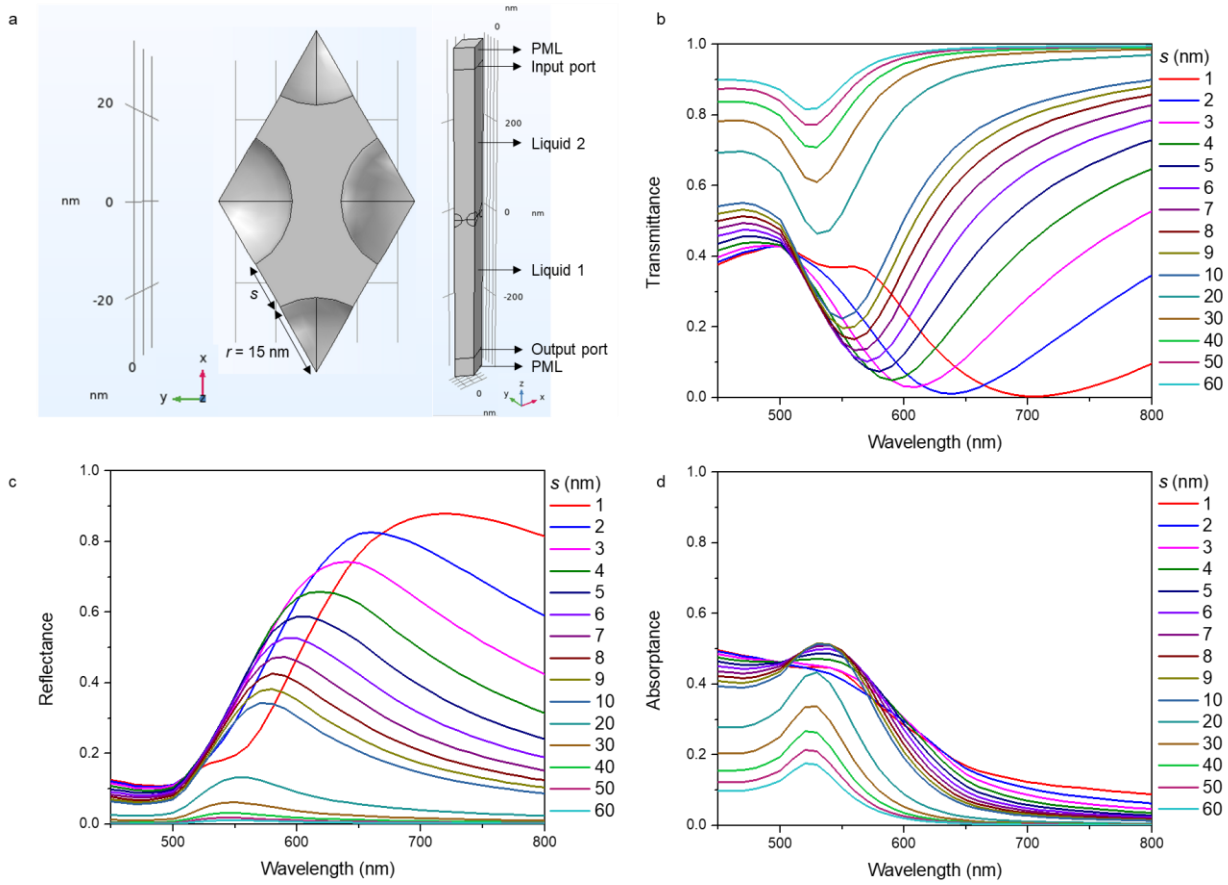

Figure S11. (a) Unit cell of an Au NP hexagonal array in top view (left) and side view (right). (b-d) Transmittance, reflectance and absorptance of Au NP hexagonal arrays with respect to the interparticle spacing, *s*.

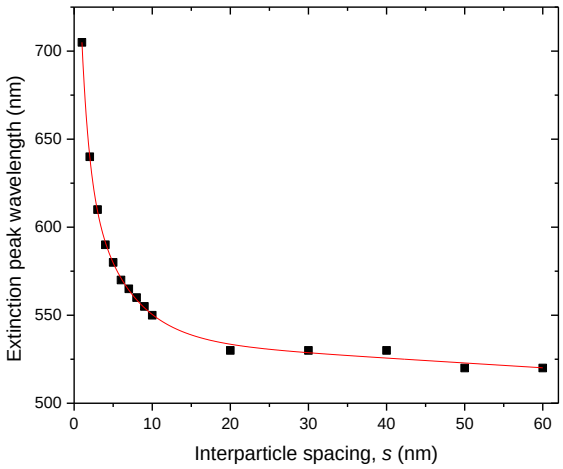

Figure S12. Extinction peak wavelength of Au NP array with respect to interparticle spacing, s.

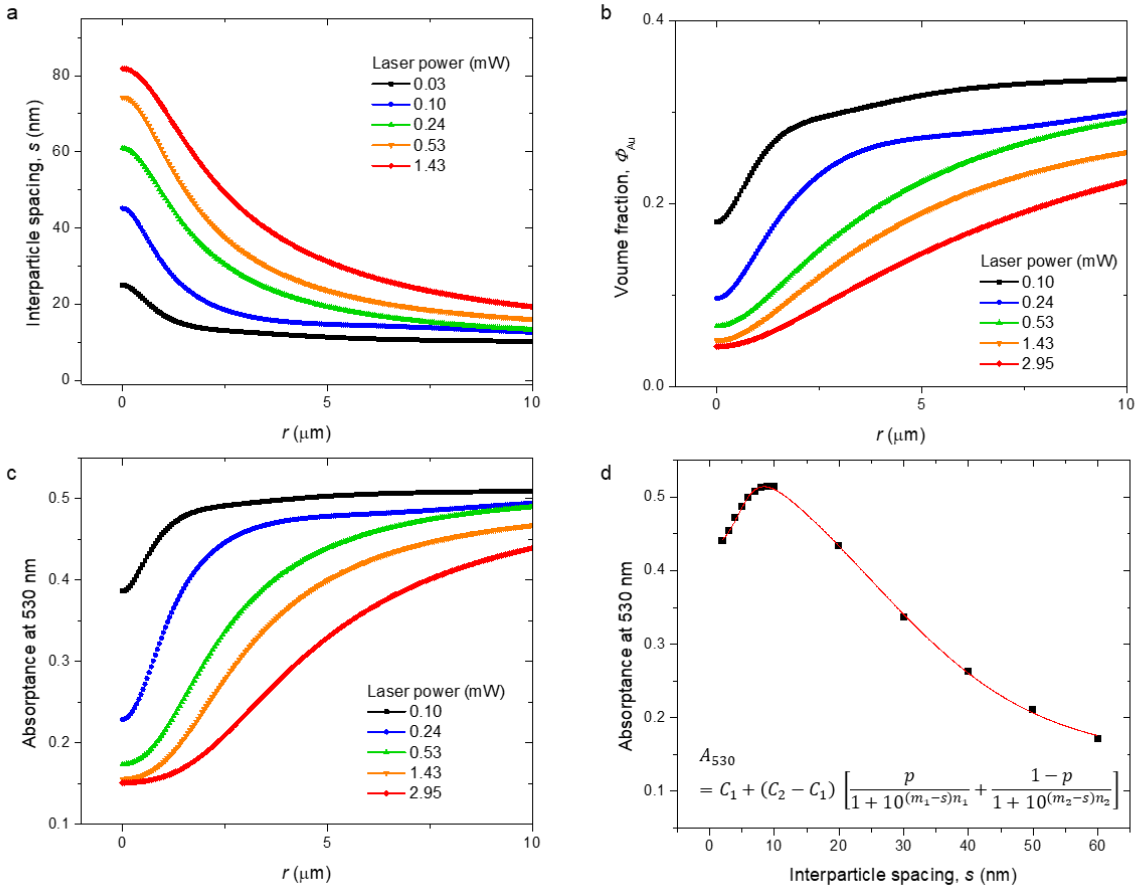

Figure S13. Derived distributions of (a) interparticle spacing, s, (b) volume fraction in a 30 nm-thick interface, Φ_{Au}, (c) absorptance at 530 nm, A, and (d) absorptance at 530 nm with respect to interparticle spacing, s.

Note S4. Calculation of effective thermal conductivity of Au NP layer

To conduct heat-involved simulations, a function of effective thermal conductivity of Au NP layer in terms of the radial distribution of Au NPs is needed. This is because the thermal conductivity of an Au NP array differs from that of a continuous gold film. The relation function was empirically found by matching measured and simulated temperature profiles. First, an interface was assumed to have the thickness of 30 nm, the diameter of Au NP, composed of Au NPs and liquid (Figure S14a). The volume fraction of Au NPs in this slab can be evaluated by taking the interparticle spacing (2.4 nm) value from the extinction peak of a dried Au NP sample (Figure S14b). The scanning electron microscopy image is shown in Figure S14c. Simulations were performed in a 3D domain consisting of a boundary between glass and water to mimic the measurement condition. At this boundary, model functions of thermal conductivity which are written with the thermal conductivities of gold and water, $k_{\mathrm{gold}}(T)$ and $k_{\mathrm{liquid}}(T)$ along with the volume fraction, Φ were applied as a boundary conductivity property[7–9]. A boundary heat source, $A \cdot I(r)$ was used, where A (=0.446) is the absorptance at 530 nm determined from the interparticle spacing of 2.4 nm and $I(r)$ is the Gaussian beam equation (Eq. 2). Putting the evaluated Φ of 0.52 and using thermally thin approximation (only in-plane conductivity), the best effective thermal conductivity, k_{eff} as a function of Φ, k_{gold} and k_{water} was found as follows (Eq. S4):

$$k_{\mathrm{eff}}\left(\Phi, k_{\mathrm{gold}}, k_{\mathrm{liquid}}\right) = \Phi\, k_{\mathrm{gold}}(T) + (1-\Phi)\, k_{\mathrm{liquid}}(T) + \frac{\Phi(1-\Phi)}{2}\left[k_{\mathrm{gold}}(T) - k_{\mathrm{liquid}}(T)\right]$$

The measured and simulated temperature profiles are shown in Figure S14d.

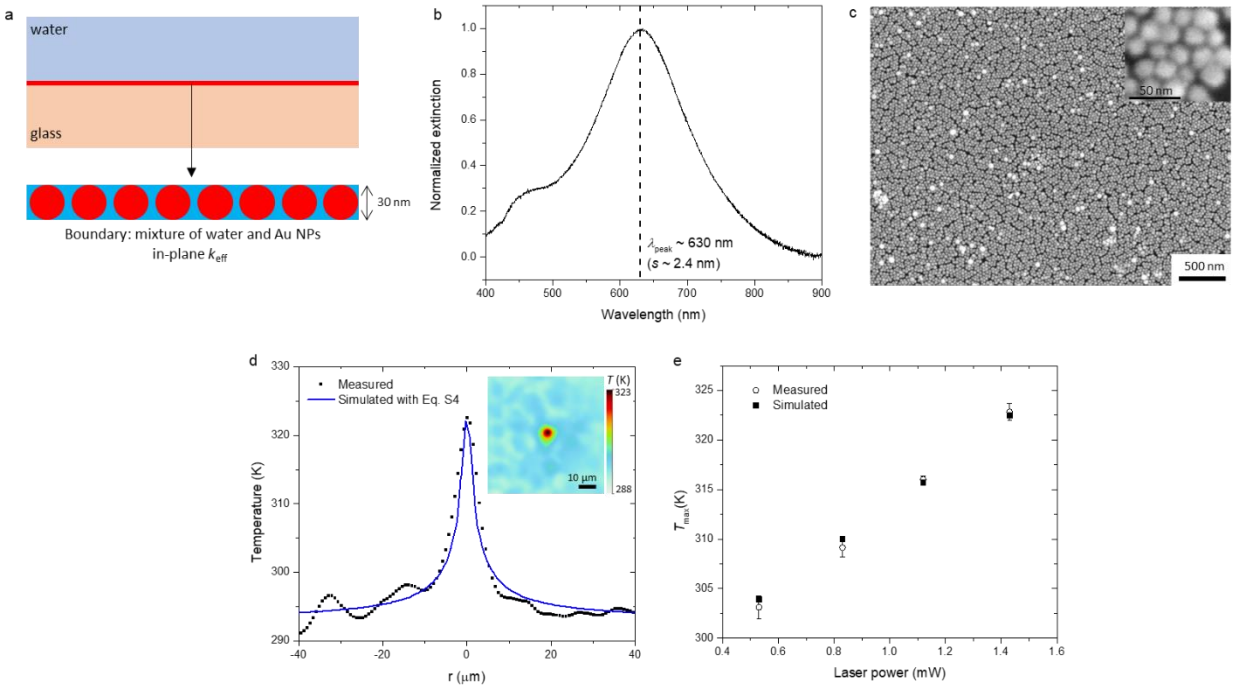

Figure S14. (a) Illustration of boundary volume containing Au NPs. (b) Extinction spectrum and (c) Scanning electron microscopy image of dried Au NPs on a glass substrate prepared by evaporating solvents of a gold interface sample. (d) Measured and simulated temperature profiles at 1.43 mW laser power. (e) Comparison between measured and simulated temperature profiles.

Note S5. Contribution of HFE droplets' thermophoretic property to the interfacial tension

The trapping behavior of microscale HFE droplets remnant on the gold interface (Movie S3) indicates the thermophobic property of these droplets in the water-ethanol medium at a wide range of temperature. Please note that a weak, outward optical gradient force is exerted on the droplets since the refractive index of HFE (1.28) is lower than that of the surrounding (1.36). Such behavior was observed for perfluoropentane droplets in water and water-ethanol media (Figure S9)[10]. In this system, long-range accumulation of droplets around a hot spot (i.e., local laser heating) was observed, implying that the thermophoretic trapping potential is relatively wide. Given these facts, we hypothesized that the temperature gradient along the interface induces accumulation of HFE-rich microemulsion droplets whose concentration contributes to the interfacial tension (Figure S15a). The term microemulsion refers to droplets of 10-200 nm size in general.

The thermophoretic force, $\mathbf{F}_{\mathrm{th}}$ acting on a particle under a temperature gradient ∇T is described with a Soret coefficient (S_T) and average temperature around the particle (T) as

$$\mathbf{F}_{\mathrm{th}} = -k_{\mathrm{B}} T S_T \nabla T, \qquad \text{(Eq. S5)}$$

where k_{B} is the Boltzmann constant.

The majority of solid particles and liquid droplets in native liquid have a thermophobic nature above around 30 °C, which means positive S_T[11,12]. The only case of negative S_T over a wide range of temperature, which was observed in our system, was reported for 1 μm phosphoglycerol-based vesicles[12]. The temperature-dependent S_T in this reference ranges from -0.4 to -0.1 K^{-1}, whose magnitude is comparable to S_T of alkane microemulsions[13,14]. Thus, we adopted the empirical formula of these S_T data to estimate the thermophoretic force and potential in our system:

$$S_T(T) = S_{T,\infty}\left[1 - \exp\left(\frac{T^* - T}{T_0}\right)\right] \qquad \text{(Eq. S6)}$$

with $S_{T,\infty} = 8.42 \times 10^3\ \mathrm{K}^{-1}$, $T^* = 367$ K, and $T_0 = 2.91 \times 10^6$ K.

Thermophoretic potentials, U_{th}, calculated using the temperature profiles in Figure 5c are shown in Figure S15b. As the laser power increases, the width and depth of the potential well increases. To relate these potential profiles to the interfacial tension, we supposed that the interfacial tension decays monoexponentially with respect to the volume fraction of microemulsions (Φ_{emulsion}) at the interface, which can be written as

$$\gamma = \gamma_{\mathrm{clean}} \exp\left(-C\Phi_{\mathrm{emulsion}}\right), \qquad \text{(Eq. S7)}$$

where γ_{clean} is the interfacial tension without interfacial emulsion and C is a scaling coefficient. By estimating $\Phi_{\mathrm{emulsion}} = 0.45$ (from density and volume changes) and putting the transient interfacial tension obtained from the pendant drop method (5.4 mN/m at 20 °C, Figure S15c) as γ_{clean} and the estimated tension for the emulsified interface (0.1 μN/m, Figure 2e), C is calculated to be 24.2. By setting 10 $k_{\mathrm{B}}T$ as the maximum potential energy at which the microemulsion droplets are closely packed ($\Phi_{\mathrm{emulsion}} = 0.74$) and zero potential energy for the

nonthermal status (Φ_{emulsion}= 0.45), the relationship between Φ_{emulsion} and U_{th} is derived as Eq. S8. The maximum potential of 10 $k_{\text{B}}T$ was used as it is considered as the potential needed for stable trapping in optical tweezers [15,16].

$$\Phi_{\text{emulsion}} = 0.45 + (0.74 - 0.45)\left(\frac{U_{\text{th}}}{10k_{\text{B}}T}\right)^2 \qquad \text{(Eq. S8)}$$

The contribution factor of the thermal droplet accumulation to the interfacial tension is further derived as follows:

$$\gamma/\gamma_0 = \exp\left[-24.2 \times 10^{-2}(0.74 - 0.45)\left({}^{U_{\text{th}}}/_{k_BT}\right)^2\right] \qquad \text{(Eq. S9)}$$

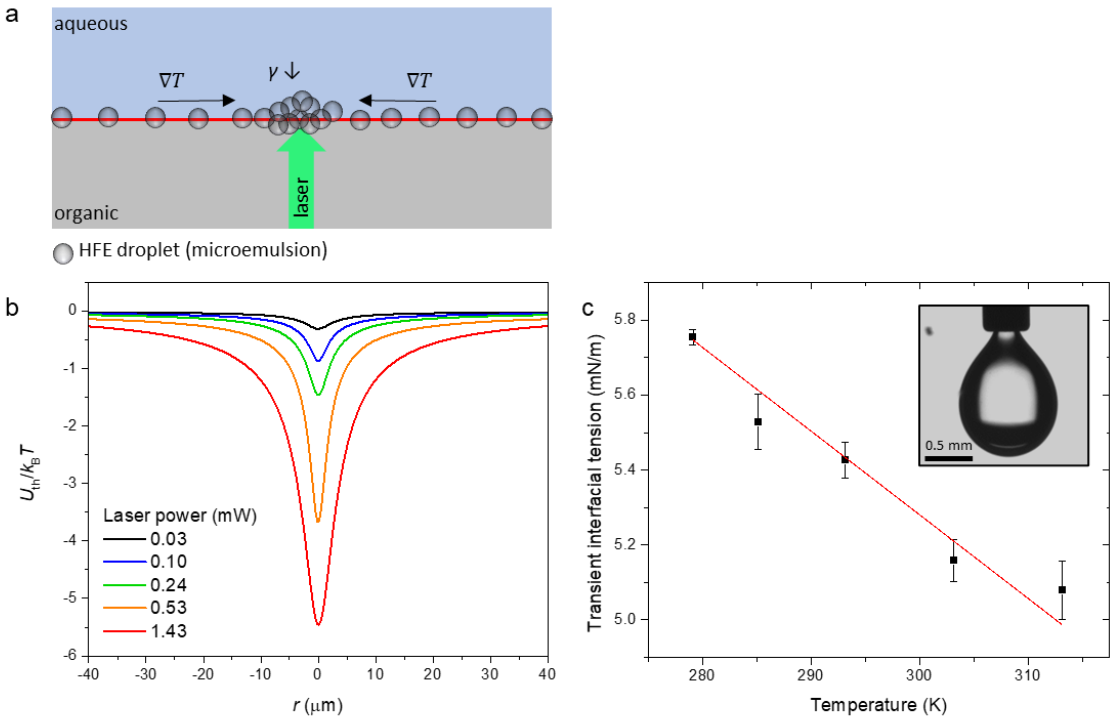

Figure S15. (a) Schematic illustration of thermophoretic accumulation of HFE droplets at the interface. (b) Calculated potentials of thermophoretic trap at different laser powers. (c) Transient interfacial tension (obtained before fall-down) with respect to temperature measured by pendant drop tensiometry (HFE drop in a water-ethanol mixture).

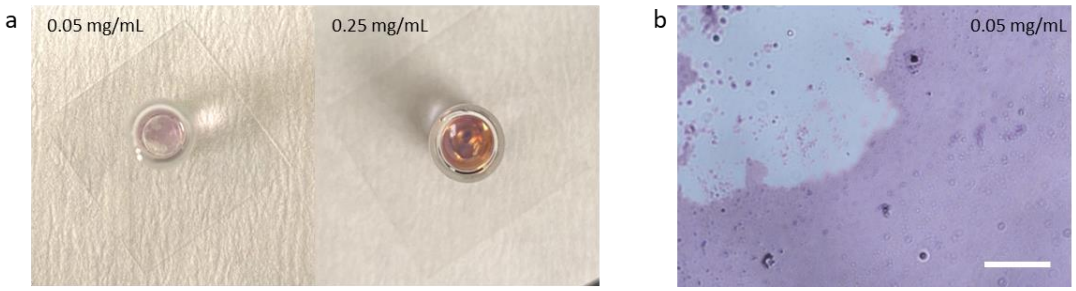

Figure S16. (a) Top view of interfaces prepared with varying concentrations of Au NPs. (b) Microscopic image of the interface prepared at a concentration of 0.05 mg/mL (scale bar: 40 μm).

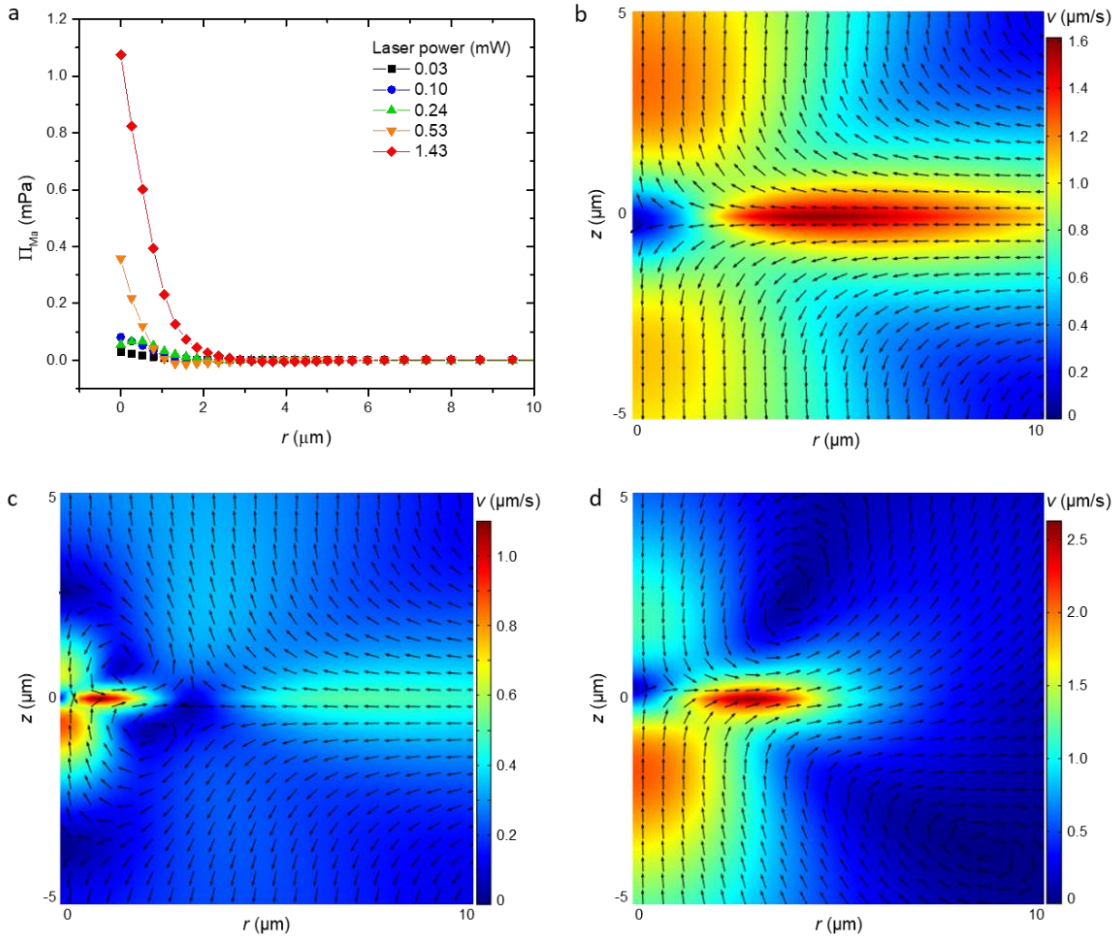

Figure S17. (a) Marangoni pressure along the interface at varying laser powers. (b-d) Simulated flow fields at different optical powers: 0.24 (b), 0.53 (c) and 1.43 mW (d). The *z*-axis is the symmetry axis (beam axis), and the *x*-axis is the liquid-liquid interface. Arrows are normalized velocity for better visualization of flow directions.

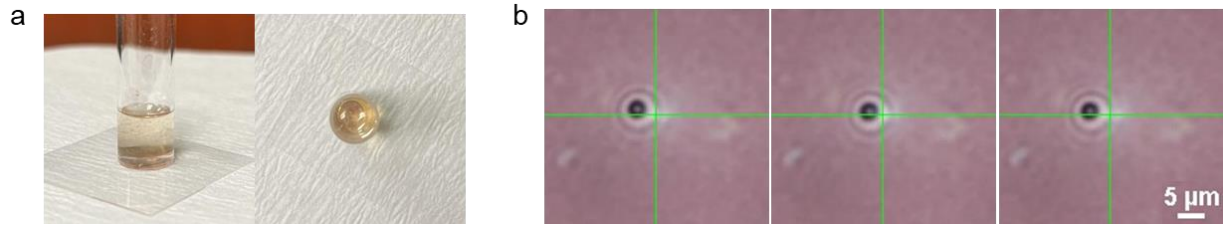

Figure S18. (a) Interfacial assembly of 30 nm silver nanoparticles under the same conditions used for gold interface samples preparation. (b) Oscillation of a PS microparticle at a distance from a 1.43 mW laser beam. Given the lower absorptance of silver nanoparticles at 532 nm compared to gold nanoparticles, the reduced optical heating at the silver interface results in a shift of particle dynamics towards lower-power regimes relative to the gold interface.

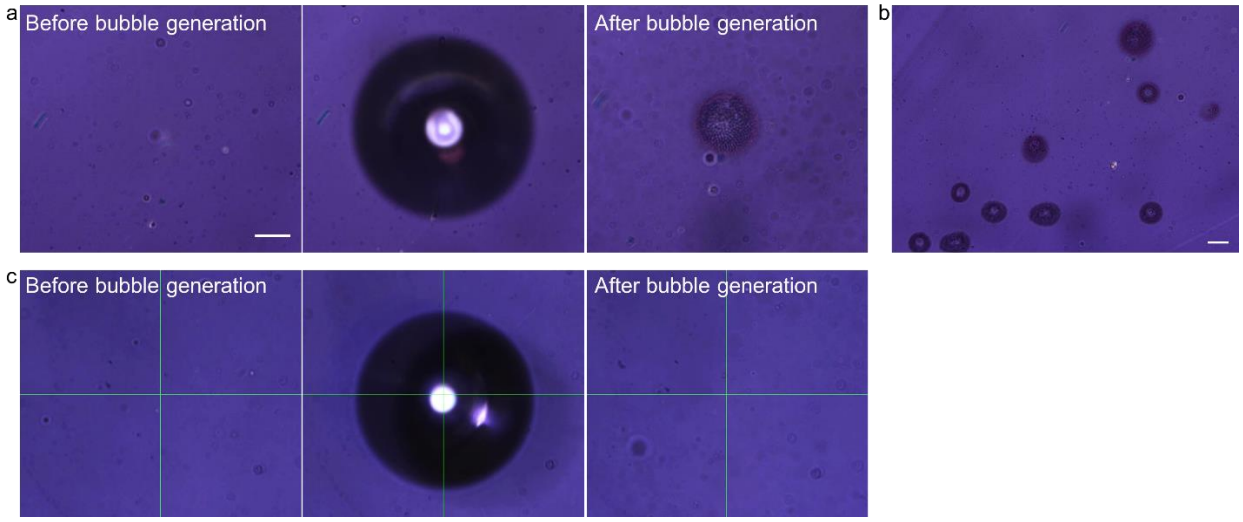

Figure S19. (a) Bubble-mediated sol-gel reaction of tetraethyl orthosilicate (TEOS). 300 mM TEOS and 1 mM NH4OH were added to the prepared gold interface samples. (b) Reaction products formed through repeated bubble generation. (c) Bubble formation observed in a sample without the addition of TEOS and NH_4OH, where the interface remains clear post-bubble formation. Scale bars: 20 µm.

Note S6. List of the functions used for the gold interface

$\rho_{\mathrm{HFE}}(T) = 2.28 \times 10^3 \; - \; 4.73\,T \; + \; 1.03 \times 10^{-2}\,T^2 \; - 1.39 \times 10^{-5}\,T^3$ [kg m^{-3}] [17]

$\rho_{\mathrm{ethanol}}(T) = 4.75 \times 10^2 + 4.71\,T - \; 1.76 \times 10^{-2}\,T^2 + 1.84 \times 10^{-5}\,T^3$ [kg m^{-3}]

$\rho_1(T) = 0.87\,\rho_{\mathrm{HFE}}(T) + 0.13\,\rho_{\mathrm{ethanol}}(T)$

$\rho_2(T) = \rho_{\mathrm{water+ethanol}}(T) = 6.82 \times 10^3 - 5.86 \times 10^1\,T + 1.96 \times 10^{-1}\,T^2 - 2.22 \times 10^{-3}\,T^3$ [kg m^{-3}]

$\Delta\rho(T,r) = \rho_1(T(r)) - \rho_2(T(r))$

$n_{\mathrm{HFE}}(T) = 1.282 - 4.38 \times 10^{-4}\,(T - 298.15)$ [18]

$n_{\mathrm{ethanol}}(T) = 1.364 - 3.90 \times 10^{-4}\,(T - 293.15)$ [19]

$n_1(T) = 0.87\,n_{\mathrm{HFE}}(T) + 0.13\,n_{\mathrm{ethanol}}(T)$

$n_2(T) = n_{\mathrm{water+ethanol}}(T) = 1.460 - 3.37 \times 10^{-4}\,T$ [20]

$\varphi_{\mathrm{Au}} = \frac{2\pi a^2}{\sqrt{3}(2a+s)^2}$ (areal coverage of Au NPs with radius *a* and interparticle spacing *s*)

$\Phi_{\mathrm{Au}} = \frac{4\pi a^3}{3\sqrt{3}a(2a+s)^2}$ (volume fraction of Au NPs with radius *a* and interparticle spacing *s* in the interfacial volume of thickness 2*a*)

$\gamma_0(T) = 2.06 \times 10^{-7} - 3.63 \times 10^{-10}\,T$ [N/m]

$\gamma(T,r) = \gamma_0\big(T(r)\big)(1 - \varphi_{\mathrm{Au}})\exp\left[-24.2 \times 10^{-2}(0.74 - 0.45)\left({}^{U_{\mathrm{th}}}\!/_{k_B T}\right)^2\right]$

$Q = A(r)I(r)$ (*Q*: interfacial heat source, *A*(*r*): absorptance at 530 nm determined in Figure S13, and *I*(*r*): Gaussian beam equation in Eq. 2)

$F_{z,Au}(T,r) = [(0.91422 + 1.4959(n_2(T) - n_1(T)) - 3.91026(n_2(T) - n_1(T))^2)]\; 2.35 \times 10^{-15}\,\pi\omega_0^2\,I(r)$ [N]

$\Pi_{\mathrm{rad,Au}}(T,r) = \frac{F_{z,Au}(T,r)}{4\pi r^2}\cos(\arctan(h'(r))$ [Pa]

$\Pi_{\mathrm{rad}}(T,r) = \varphi_{\mathrm{Au}}\Pi_{\mathrm{rad,Au}}(T,r) + (1 - \varphi_{\mathrm{Au}})\Pi_{\mathrm{rad,LL}}(T,r)$ ($\Pi_{\mathrm{rad,LL}}$ from Eq. S3)

Captions for Movies S1-7

Movie S1. Motion of PS particles clustered on an Au NP-loaded liquid-liquid interface upon laser illumination.

Movie S2. Motion of PS particles upon laser illumination in different liquid systems: gold interface, bare liquid-liquid interface, and monophasic liquid (water-ethanol mixture).

Movie S3. Optothermal trapping of remnant HFE droplets on an Au NP-loaded liquid-liquid interface.

Movie S4. Motion of a PS particle upon laser illumination on a deposited film of Au NPs and on an interface prepared at high concentration.

Movie S5. Release of accumulated droplets upon deactivation of the laser after actuation and bubble formation at the interface.

Movie S6. Trapping of PS particles with various sizes and materials.

Movie S7. Bubble-mediated sol-gel reaction of TEOS.

References

(1) Girot, A.; Petit, J.; Saiseau, R.; Guérin, T.; Chraibi, H.; Delabre, U.; Delville, J. P. Conical Interfaces between Two Immiscible Fluids Induced by an Optical Laser Beam. *Phys. Rev. Lett.* **2019**, *122* (17), 174501. https://doi.org/10.1103/PhysRevLett.122.174501.

(2) Wunenburger, R.; Casner, A.; Delville, J. P. Light-Induced Deformation and Instability of a Liquid Interface. I. Statics. *Phys. Rev. E - Stat. Nonlinear, Soft Matter Phys.* **2006**, *73* (3), 1–16. https://doi.org/10.1103/PhysRevE.73.036314.

(3) An, N.; Zhuang, B.; Li, M.; Lu, Y.; Wang, Z. G. Combined Theoretical and Experimental Study of Refractive Indices of Water-Acetonitrile-Salt Systems. *J. Phys. Chem. B* **2015**, *119* (33), 10701–10709. https://doi.org/10.1021/acs.jpcb.5b05433.

(4) Sakai, T. Surfactant-Free Emulsions. *Curr. Opin. Colloid Interface Sci.* **2008**, *13* (4), 228–235. https://doi.org/10.1016/j.cocis.2007.11.013.

(5) dos Santos Lucas, C. R.; Aum, Y. K. P. G.; de Andrade Araújo, E.; de Castro Dantas, T. N.; Araújo, E. A.; Sousa, T. N.; Aum, P. T. P. Investigating the Fluid-Solid Interaction of Acid Nonionic Nanoemulsion with Carbonate Porous Media. *Molecules* **2020**, *25* (6). https://doi.org/10.3390/molecules25061475.

(6) Maciel, N. R.; Oliveira, E. C. V.; Okuma, C. H.; Topan, J. F.; Amaral, L. Q.; Rocha-Filho, P. A New System of Multiple Emulsions with Lamellar Gel Phases from Vegetable Oil. *J. Dispers. Sci. Technol.* **2016**, *37* (5), 646–655. https://doi.org/10.1080/01932691.2015.1054506.

(7) Bird, R. B.; Stewart, W. E.; N., L. E. *Transport Phenomena*, 2nd ed.; John Wiley & Sons, Inc., 2006.

(8) Kiradjiev, K. B.; Halvorsen, S. A.; Van Gorder, R. A.; Howison, S. D. Maxwell-Type Models for the Effective Thermal Conductivity of a Porous Material with Radiative Transfer in the Voids. *Int. J. Therm. Sci.* **2019**, *145* (June), 106009. https://doi.org/10.1016/j.ijthermalsci.2019.106009.

(9) Levy, F. L. A Modified Maxwell-Eucken Equation for Calculating the Thermal Conductivity of Two-Component Solutions or Mixtures. *Int. J. Refrig.* **1981**, *4* (4), 223–225. https://doi.org/10.1016/0140-7007(81)90053-0.

(10) Kim, Y.; Ding, H.; Zheng, Y. Investigating Water/Oil Interfaces with Opto-Thermophoresis. *Nat. Commun.* **2022**, *13* (1), 3742. https://doi.org/10.1038/s41467-022-31546-3.

(11) Kollipara, P. S.; Li, X.; Li, J.; Chen, Z.; Ding, H.; Kim, Y.; Huang, S.; Qin, Z.; Zheng, Y. Hypothermal Opto-Thermophoretic Tweezers. *Nat. Commun.* **2023**, *14* (1), 1–9. https://doi.org/10.1038/s41467-023-40865-y.

(12) Talbot, E. L.; Kotar, J.; Parolini, L.; Di Michele, L.; Cicuta, P. Thermophoretic Migration of Vesicles Depends on Mean Temperature and Head Group Chemistry. *Nat. Commun.* **2017**, *8* (May), 1–8. https://doi.org/10.1038/ncomms15351.

(13) Vigolo, D.; Brambilla, G.; Piazza, R. Thermophoresis of Microemulsion Droplets: Size

Dependence of the Soret Effect. *Phys. Rev. E - Stat. Nonlinear, Soft Matter Phys.* **2007**, *75* (4), 1–4. https://doi.org/10.1103/PhysRevE.75.040401.

(14) Naumann, P.; Datta, S.; Sottmann, T.; Arlt, B.; Frielinghaus, H.; Wiegand, S. Isothermal Behavior of the Soret Effect in Nonionic Microemulsions: Size Variation by Using Different n -Alkanes. *J. Phys. Chem. B* **2014**, *118* (12), 3451–3460. https://doi.org/10.1021/jp412126n.

(15) Favre-Bulle, I. A.; Stilgoe, A. B.; Scott, E. K.; Rubinsztein-Dunlop, H. Optical Trapping in Vivo: Theory, Practice, and Applications. *Nanophotonics* **2019**, *8* (6), 1023–1040. https://doi.org/10.1515/nanoph-2019-0055.

(16) Kotsifaki, D. G.; Chormaic, S. N. Plasmonic Optical Tweezers Based on Nanostructures: Fundamentals, Advances and Prospects. *Nanophotonics* **2019**, *8* (7), 1227–1245. https://doi.org/10.1515/nanoph-2019-0151.

(17) Rausch, M. H.; Kretschmer, L.; Will, S.; Leipertz, A.; Fröba, A. P. Density, Surface Tension, and Kinematic Viscosity of Hydrofluoroethers HFE-7000, HFE-7100, HFE-7200, HFE-7300, and HFE-7500. *J. Chem. Eng. Data* **2015**, *60* (12), 3759–3765. https://doi.org/10.1021/acs.jced.5b00691.

(18) Faoro, R.; Bassu, M.; Burg, T. P. Determination of the Refractive Index of Liquids at Cryogenic Temperature. *Appl. Phys. Lett.* **2018**, *113* (8). https://doi.org/10.1063/1.5043370.

(19) Sheldon, S. J.; Knight, L. V.; Thorne, J. M. Laser-Induced Thermal Lens Effect: A New Theoretical Model. *Appl. Opt.* **1982**, *21* (9), 1663. https://doi.org/10.1364/ao.21.001663.

(20) Nowakowska, J. The Refractive Indices of Ethyl Alcohol and Water Mixtures, Loyola University Chicago, 1939.